

Chapter 5

Lightly Fluorinated Graphene as a Barrier Layer to n-type Si(111) Photoanodes

5.1 Background and Introduction

The behavior of n-Si(111) photoanodes covered by monolayer sheets of fluorinated graphene (F-Gr) was investigated under a range of chemical and electrochemical conditions. The electrochemical behavior of n-Si/F-Gr and np⁺-Si/F-Gr photoanodes was compared to hydride-terminated n-Si (n-Si-H) electrodes in contact with aqueous Fe(CN)₆^{3-/4-} and Br₂/HBr electrolytes as well as in contact with a series of outer-sphere, one-electron redox couples in nonaqueous electrolytes. Illuminated n-Si/F-Gr and np⁺-Si/F-Gr electrodes in contact with an aqueous [K₃(Fe(CN)₆]/[K₄(Fe(CN)₆)] exhibited stable short-circuit photocurrent densities of ~10 mA cm⁻² for > 100,000 s (>24 hours), in comparison to bare Si electrodes, which yielded nearly a complete photocurrent decay over ~100 s. X-ray photoelectron spectra collected before and after exposure to aqueous anodic conditions showed that oxide formation at the Si surface was significantly inhibited for Si electrodes coated with F-Gr relative to bare Si electrodes exposed to the same conditions. The variation of the open-circuit potential for n-Si/F-Gr in contact with a series of nonaqueous electrolytes of varying reduction potential indicated that the n-Si/F-Gr did not form a buried junction with respect to the solution

contact. Further, illuminated n-Si/F-Gr electrodes in contact with $\text{Br}_2/\text{HBr}(\text{aq})$ were significantly more stable than n-Si-H electrodes over three cyclic voltammetry sweeps, and n-Si/F-Gr electrodes coupled to a Pt catalyst exhibited ideal regenerative cell efficiencies of up to 5% for the oxidation of Br^- to Br_2 .

Several protective coating strategies have been developed to suppress deleterious surface reactions associated with corrosion or passivation of semiconductor photoanodes in aqueous electrolytes.^{1,2} Nickel Oxide (NiO_x) films prepared by reactive sputtering or amorphous TiO_2 films in conjunction with a NiO_x based electrocatalyst have produced extended stability for Si photoanodes and allow the photochemical evolution of $\text{O}_2(\text{g})$ from water under alkaline conditions.^{3,4} Thin metallic overlayers or transparent conductive metal oxide protective layers often result in relatively low photovoltages due to thermionic emission of majority carriers at Si/overlayer Schottky contacts.³⁻¹⁰ Insulating metal oxide barriers must be thin enough (a few nm) to permit conduction by tunneling, and such thin layers are difficult to prepare in a pinhole-free manner over macroscopic areas.^{5,11,12} Chemical functionalization has led to improved stability of n-Si surfaces, but such methods have not yet yielded stability over extended time periods in aqueous electrolytes.¹³⁻¹⁵

An ideal protective coating would be transparent, provide low resistance to charge transfer, allow for maximum energy-conversion efficiency for a range of semiconductor/electrolyte contacts, be applied easily to semiconductor surfaces, be capable of uniformly protecting macroscopic electrode areas, and be chemically and electrochemically stable under the relevant conditions. Monolayer graphene can be prepared in large ($>100 \text{ cm}^2$), pinhole-free layers and transferred to any arbitrary planar

surface, and has been shown to inhibit oxidation of metals both in air and in aqueous solution.¹⁶⁻²¹ Graphene is chemically inert, optically transparent, can be deposited onto surfaces at room temperature. Illuminated graphene-coated Si photoanodes in contact with neutral pH aqueous electrolytes have demonstrated stability for over 1000 s while providing desirable photoelectrochemical performance.²²⁻²⁵ However, the graphene does not completely protect the Si photoanodes from oxidation, and the devices exhibit partial Fermi-level pinning, which limits their energy-conversion efficiency. The incomplete protection and Fermi-level pinning are consistently ascribed to reactive sites near grain boundaries in the polycrystalline graphene produced by chemical-vapor deposition (CVD), and to the presence of mid-gap electronic states introduced at the n-Si/Gr interface as a result of the graphene electronic structure, respectively.

Relative to unfluorinated graphene, fluorination of graphene should reduce the density of states near the Fermi level, thus reducing Fermi level pinning effects, and should passivate reactive graphene defect sites via fluorine capping.²⁶⁻²⁸ Accordingly, we report herein an investigation of the stability and photoelectrochemical behavior of fluorinated-graphene-coated Si photoanodes in contact with aqueous electrolytes.

5.2 Behavior of fluorinated-graphene-covered n-Si photoelectrodes

5.2.1. Stability of F-Gr covered n-Si surfaces in aqueous solution

Detailed experimental procedures are provided in the chapter 5 appendix. Briefly, monolayer sheets of lightly fluorinated graphene (<10 atom% F) were fabricated by treating CVD-grown graphene on a Cu foil with $\text{XeF}_2(\text{g})$.²⁸ X-ray photoelectron spectroscopy (XPS) of the resulting F-Gr confirmed the fluorination.^{27,28} The F-Gr was further characterized by UV/Vis and Raman spectroscopy (see SI). The fluorinated graphene sheets were transferred to n-Si and np^+ -Si electrodes using standard CVD graphene growth and transfer methods.^{29,30}

Figure 5.1 shows the current-density vs. time ($J-t$) and current density vs. potential ($J-E$) behavior for illuminated ($\sim 33 \text{ mW cm}^{-2}$ ENH-type W-halogen lamp) n-Si/F-Gr photoanodes in contact with aqueous $50 \text{ mM Fe}(\text{CN})_6^{3-} - 350 \text{ mM Fe}(\text{CN})_6^{4-}$ (aq). The n-Si/F-Gr electrodes exhibited stable current over 100 s while the current density of n-Si-H electrodes decayed to nearly baseline values over the same time period (Figure 5.1a). Furthermore, the current density of the n-Si/F-Gr electrode decayed by less than 1 mA cm^{-2} over 100,000 s of continuous operation (Figure 5.1b). After correcting for fluctuations in the light intensity impinging on the electrode, greater than 97% of the expected current density of an ideally stable electrode was observed. Similar results were observed for np^+ -Si/F-Gr electrodes (see appendix). Figure 5.1c depicts the $J-E$ behavior before and after exposure to the conditions in Figure 5.1b. The stable open-circuit

potential (-0.27 V vs. $E(A/A^-)$) and fill factor (ff , 0.33 before exposure, 0.32 after exposure) attest to the stability of the n-Si/F-Gr interface.

Prior to the stability test, the open-circuit potential (E_{oc}) of the n-Si/F-Gr electrode was -0.27 V vs. $E(A/A^-)$, approximately 70 mV lower than the reported E_{oc} of -0.34 V vs. $E(A/A^-)$ for n-Si coated with a single layer of graphene.²² Further, exposure of n-Si/F-Gr to a series of non-aqueous electrolytes of varying electrochemical potential showed a dependence of E_{oc} on $E(A/A^-)$, indicating partial Fermi level pinning of the n-Si surface with respect to the solution potential. The mutually similar fill factors (ff) of the n-Si/F-Gr electrode and np^+ -Si/F-Gr electrodes, 0.33 and 0.30, respectively (Figure 5.1c, Figure 5A.1), indicated similar limiting resistance to charge transfer in both systems.

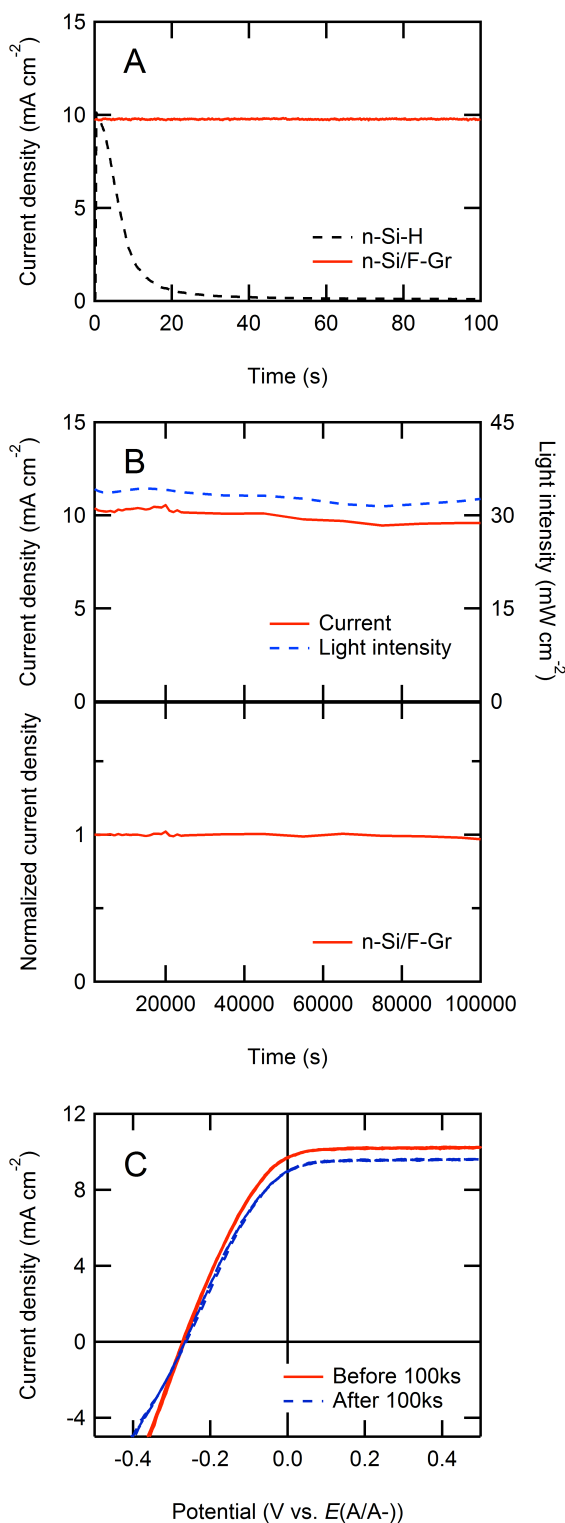


Figure 5.1. Current density-time ($J-t$) and current density-potential ($J-E$) behavior of n-Si/F-Gr electrodes in contact with aqueous 50 mM $\text{Fe}(\text{CN})_6^{3-}$ - 350 mM $\text{Fe}(\text{CN})_6^{4-}$ under $\sim 33 \text{ mW cm}^{-2}$ of ENH-type W-halogen lamp illumination. (A) Comparison of the $J-t$ behavior of bare n-Si-H and n-Si/F-Gr electrodes over 100 s. (B) The $J-t$ behavior of F-Gr covered n-Si at $E = 0 \text{ V}$ vs. the Nernstian potential of the solution ($E(A/A^-)$) over 100,000 s (>24 hours). The normalized current density is reported to correct for any variation in the intensity of the light source with time. (C) $J-E$ behavior of n-Si/F-Gr (3 scans at 50 mV s^{-1}) before and after exposure to the conditions depicted in (B).

5.2.2. Inhibition of silicon oxide formation at F-Gr-covered n-Si surfaces

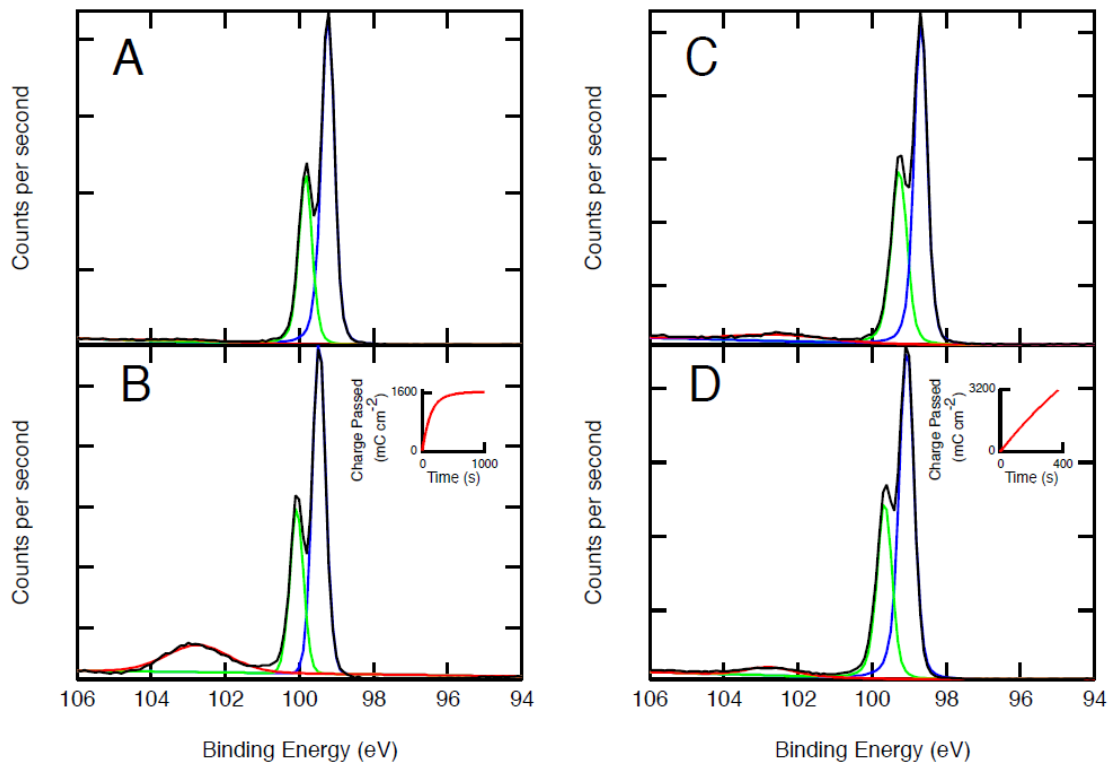


Figure 5.2. XP spectra of n-Si-Me and n-Si-Me/F-Gr electrodes. (A) and (B) show the XP spectra of an n-Si-Me electrode before and after passing 1600 mC cm^{-2} (inset) while passing anodic current in contact with an aqueous 50 mM $\text{Fe}(\text{CN})_6^{3-}$ - 350 mM $\text{Fe}(\text{CN})_6^{4-}$ electrolyte. (C) and (D) show an n-Si-Me/F-Gr electrode before and after passing 3200 mC cm^{-2} under similar electrochemical conditions to (A) and (B).

Figure 5.2 shows a comparison of the XP spectra of methyl-terminated n-Si electrodes (n-Si-Me) with and without a F-Gr protective layer before and after photoelectrochemical testing in an aqueous 50 mM $\text{Fe}(\text{CN})_6^{3-}$ - 350 mM $\text{Fe}(\text{CN})_6^{4-}$ electrolyte. After passing 1600 mC cm^{-2} of anodic charge on an n-Si-Me electrode, the growth of an oxide peak was observed in the Si 2p XPS region and was consistent with formation of multiple layers of oxide. In contrast, no additional growth of the oxide peak was observed after passing twice the number of Coulombs (3200 mC cm^{-2}) across an n-Si-Me/F-Gr electrode (See appendix). Hence, F-Gr acts as a physical barrier to oxide formation, preserving the photoelectrochemical behavior of the n-Si-Me/solution interface. Methylated surfaces were used because, in contrast with n-Si-H surfaces, the n-Si-Me surface does not easily oxidize in air nor forms significant oxide upon fabrication of n-Si/F-Gr interfaces, allowing more facile observation of oxide growth in the presence various protective layers, such as F-Gr. F-Gr covered Si surfaces did not form platinum silicide upon evaporation of Pt onto the F-Gr/Si surface, and F-Gr is stable in both aqueous and acidic (pH 0) solutions, suggesting F-Gr also provides as an effective physical barrier to inhibit Pt/Si reactivity and is stable under harsh fabrication and electrolyte conditions (see appendix).

5.2.3. Photoelectrochemical behavior of F-Gr/n-Si interfaces under bromide oxidation conditions

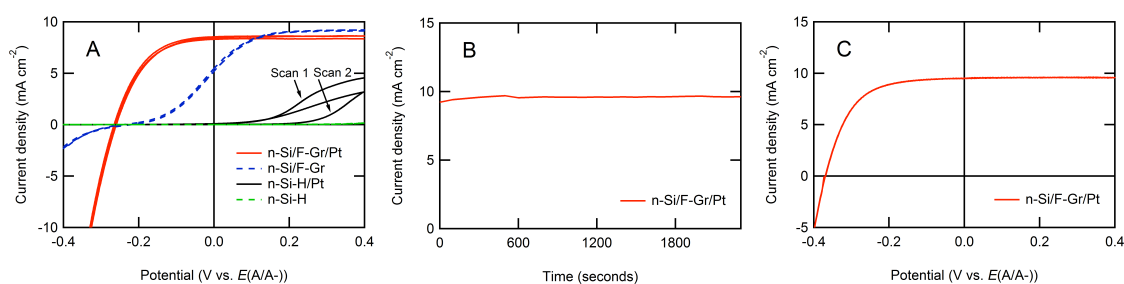


Figure 5.3. Electrochemical behavior of n-Si/F-Gr and n-Si-H electrodes with and without Pt deposition in aqueous 0.4 M Br₂ – 7.0 M HBr (pH = 0) electrolyte under 33 mW cm⁻² from an ELH-type W-halogen lamp). (A) *J-E* behavior of n-Si/F-Gr and n-Si-H electrodes with and without Pt deposition. Each cyclic voltammogram was started at +0.4 V vs. *E(A/A⁻)* and swept twice to more negative potentials at 50 mV s⁻¹. (B) *J-t* behavior of an n-Si/F-Gr/Pt electrode over 45 min at *E* = 0 V vs. *E(A/A⁻)* (C) *J-E* behavior of an n-Si/F-Gr/Pt electrode after exposure to conditions described in (B).

Figure 5.3 displays the J - E behavior of n-Si-H and n-Si/F-Gr electrodes under $\sim 33 \text{ mW cm}^{-2}$ illumination intensity in contact with 0.4 M Br_2 – 7.0 M HBr (pH=0), with and without electrochemical deposition of 100 mC cm^{-2} of a Pt catalyst, respectively. With the Pt catalyst, the properties of the n-Si/F-Gr/Pt electrode improved to E_{oc} (n-Si/F-Gr/Pt) = 0.26 V, ff = 0.52, and J_{sc} = 8.3 mA/cm^2 from E_{oc} (n-Si/F-Gr) = 0.22 V, ff = 0.16, J_{sc} = 5.14 mA cm^{-2} . The improved ff can be ascribed to improved catalysis for the Br^- to Br_2 reaction effected by the Pt. The current density of the n-Si-H/Pt electrode under illumination decayed precipitously over two potential sweeps, while the n-Si/F-Gr/Pt electrode showed a stable ff and photocurrent density under the same conditions. The n-Si/F-Gr/Pt electrode had an ideal regenerative cell efficiency (η_{IRC}) of 3.5% in contact with the Br_2/HBr (aq) electrolyte.³¹ The current density at n-Si/F-Gr/Pt electrodes was stable over 45 min at $E = 0 \text{ V}$ vs. the Nernstian potential of the solution, $E(A/A^+)$ and η_{IRC} increased to 5% over this time (See appendix). The improvement in η_{IRC} indicates a change in the energetics of the n-Si/F-Gr/Pt interface after electrochemical deposition of Pt.

5.3 Conclusion

Although only lightly fluorinated (C_xF , $x > 10$) graphene was used herein, these fluorinated graphene sheets provided superior protection against corrosion to the underlying Si relative to the protection imparted by monolayer graphene on n-Si(111) photoanodes (See appendix).²² These results are consistent with the hypothesis that light fluorination of graphene induces reaction with high-energy defect sites, such as dangling bonds or missing atoms, effectively sealing defects that otherwise would allow oxide formation at the n-Si surface and further degradation of the Gr protective layer. The

bonding of a very electronegative atom to the surface may also increase the hydrophobicity of the graphene sheet, which would further reduce deleterious corrosion reactions near pinholes.

In conclusion, fluorinated graphene forms an effective physical barrier between silicon surfaces and a number of contacting phases, including acidic and neutral pH aqueous electrolyte as well as metallic interfaces. Additionally, Si covered by fluorinated graphene exhibits partial Fermi level pinning in contact with non-aqueous electrolytes. Additional work at higher fluorination levels on both p-type and n-type silicon will elucidate whether a reduction in the density of states near the Fermi level can lead to a fully unpinned interface, and will allow elucidation of the effect of the graphene-based surface dipole on the electrochemical behavior of the resultant photoelectrode.

5.4 Acknowledgements

The bulk of this work will soon appear in publication. Annelise Thompson was an equal contributor to these efforts and I am also thankful to Chris Roske, Jackie Maslyn, Yufeng Hao and Noah Plymale for their invaluable contributions to this work.

5.5 References

1. S. Hu, N. S. Lewis, J. W. Ager, J. Yang, J. R. McKone and N. C. Strandwitz, *J. Phys. Chem. C*, 2015, **119**, 24201-24228.
2. K. Sun, S. Shen, Y. Liang, P. E. Burrows, S. S. Mao and D. Wang, *Chem. Rev.*, 2014, **114**, 8662-8719.
3. K. Sun, M. T. McDowell, A. C. Nielander, S. Hu, M. R. Shaner, F. Yang, B. S. Brunshwig and N. S. Lewis, *J. Phys. Chem. Lett.*, 2015, **6**, 592-598.
4. S. Hu, M. R. Shaner, J. A. Beardslee, M. Lichterman, B. S. Brunshwig and N. S. Lewis, *Science*, 2014, **344**, 1005-1009.
5. N. C. Strandwitz, D. J. Comstock, R. L. Grimm, A. C. Nichols-Nielander, J. Elam and N. S. Lewis, *J. Phys. Chem. C*, 2013, **117**, 4931-4936.
6. D. Bélanger, J. P. Dodelet and B. A. Lombos, *J. Electrochem. Soc.*, 1986, **133**, 1113-1119.
7. A. Q. Contractor and J. O. M. Bockris, *Electrochim. Acta*, 1984, **29**, 1427-1434.
8. A. T. Howe, R. T. Hawkins and T. H. Fleisch, *J. Electrochem. Soc.*, 1986, **133**, 1369-1375.
9. S. Menezes, A. Heller and B. Miller, *J. Electrochem. Soc.*, 1980, **127**, 1268-1273.
10. S. M. Sze and K. Ng, K., *Physics of Semiconductor Devices*, John Wiley & Sons, Inc., Hoboken, NJ, 3rd edn., 2007.
11. Y. W. Chen, J. D. Prange, S. Dühnen, Y. Park, M. Gunji, C. E. D. Chidsey and P. C. McIntyre, *Nat. Mater.*, 2011, **10**, 539-544.
12. S. J. Fonash, *Solar Cell Device Physics*, Elsevier Inc., Amsterdam, 2nd edn., 2010.

13. A. Bansal and N. S. Lewis, *J. Phys. Chem. B*, 1998, **102**, 4058-4060.
14. A. Bansal and N. S. Lewis, *J. Phys. Chem. B*, 1998, **102**, 1067-1070.
15. J. M. Bolts, A. B. Bocarsly, M. C. Palazzotto, E. G. Walton, N. S. Lewis and M. S. Wrighton, *J. Am. Chem. Soc.*, 1979, **101**, 1378-1385.
16. S. Chen, L. Brown, M. Levendorf, W. Cai, S.-Y. Ju, J. Edgeworth, X. Li, C. W. Magnuson, A. Velamakanni, R. D. Piner, J. Kang, J. Park and R. S. Ruoff, *ACS Nano*, 2011, **5**, 1321-1327.
17. G. W. Flynn, *J. Chem. Phys.*, 2011, **135**, 050901-050908.
18. Y. Lee, S. Bae, H. Jang, S. Jang, S.-E. Zhu, S. H. Sim, Y. I. Song, B. H. Hong and J.-H. Ahn, *Nano Lett.*, 2010, **10**, 490-493.
19. D. Prasai, J. C. Tuberquia, R. R. Harl, G. K. Jennings and K. I. Bolotin, *ACS Nano*, 2012, **6**, 1102-1108.
20. J. W. Suk, A. Kitt, C. W. Magnuson, Y. Hao, S. Ahmed, J. An, A. K. Swan, B. B. Goldberg and R. S. Ruoff, *ACS Nano*, 2011, **5**, 6916-6924.
21. E. Sutter, P. Albrecht, F. E. Camino and P. Sutter, *Carbon*, 2010, **48**, 4414-4420.
22. A. C. Nielander, M. J. Bierman, N. Petrone, N. C. Strandwitz, S. Ardo, F. Yang, J. Hone and N. S. Lewis, *J. Am. Chem. Soc.*, 2013, **135**, 17246-17249.
23. S. Droscher, P. Roulleau, F. Molitor, P. Studerus, C. Stampfer, K. Ensslin and T. Ihn, *Appl. Phys. Lett.*, 2010, **96**, 152104-152103.
24. L. A. Ponomarenko, R. Yang, R. V. Gorbachev, P. Blake, A. S. Mayorov, K. S. Novoselov, M. I. Katsnelson and A. K. Geim, *Phys. Rev. Lett.*, 2010, **105**, 136801.

25. S. Bae, H. Kim, Y. Lee, X. Xu, J.-S. Park, Y. Zheng, J. Balakrishnan, T. Lei, H. Ri Kim, Y. I. Song, Y.-J. Kim, K. S. Kim, B. Ozyilmaz, J.-H. Ahn, B. H. Hong and S. Iijima, *Nat. Nano.*, 2010, **5**, 574-578.
26. R. R. Nair, W. Ren, R. Jalil, I. Riaz, V. G. Kravets, L. Britnell, P. Blake, F. Schedin, A. S. Mayorov, S. Yuan, M. I. Katsnelson, H.-M. Cheng, W. Strupinski, L. G. Bulusheva, A. V. Okotrub, I. V. Grigorieva, A. N. Grigorenko, K. S. Novoselov and A. K. Geim, *Small*, 2010, **6**, 2877-2884.
27. J. T. Robinson, J. S. Burgess, C. E. Junkermeier, S. C. Badescu, T. L. Reinecke, F. K. Perkins, M. K. Zalalutdniov, J. W. Baldwin, J. C. Culbertson, P. E. Sheehan and E. S. Snow, *Nano Lett.*, 2010, **10**, 3001-3005.
28. R. Stine, W.-K. Lee, K. E. Whitener, J. T. Robinson and P. E. Sheehan, *Nano Lett.*, 2013, **13**, 4311-4316.
29. N. Petrone, C. R. Dean, I. Meric, A. M. van der Zande, P. Y. Huang, L. Wang, D. Muller, K. L. Shepard and J. Hone, *Nano Lett.*, 2012, **12**, 2751-2756.
30. Y. Hao, M. S. Bharathi, L. Wang, Y. Liu, H. Chen, S. Nie, X. Wang, H. Chou, C. Tan, B. Fallahazad, H. Ramanarayan, C. W. Magnuson, E. Tutuc, B. I. Yakobson, K. F. McCarty, Y.-W. Zhang, P. Kim, J. Hone, L. Colombo and R. S. Ruoff, *Science*, 2013, **342**, 720-723.
31. R. H. Coridan, A. C. Nielander, S. A. Francis, M. T. McDowell, V. Dix, S. M. Chatman and N. S. Lewis, *Energy Environ. Sci.*, 2015, **8**, 2886-2901.

5.6 Appendix

5.6.1 Methods

5.6.1.1 Materials

Single-crystalline, Czochralski grown, (111)-oriented, planar, 380 μm thick, phosphorus doped, 1.1 $\Omega\text{-cm}$ resistivity (doping density, $N_D \approx 5 \times 10^{15} \text{ cm}^{-3}$) single-side polished n-type silicon wafers were obtained from University Wafer, Inc. Water was obtained from a Barnstead Nanopure system and had a resistivity $\geq 18.0 \text{ M}\Omega\text{-cm}$. Copper Etch Type CE – 100 (FeCl_3 -based, Transene Company, Inc., Danvers, MA), and buffered HF(aq) (semiconductor grade, Transene Company, Inc., Danvers, MA) were used as received. Acetone (HPLC grade, Sigma-Aldrich) was used as received. Acetonitrile (99.8% anhydrous, Sigma-Aldrich) used in electrochemical measurements was dried over Al_2O_3 prior to use.

Ferrocene (Fc , bis(cyclopentadienyl)iron(II), 99%, Strem), cobaltocene (CoCp_2 , bis(cyclopentadienyl)cobalt(II), 98%, Strem), and acetylferrocene (AcFc , (acetylcyclopentadienyl)-cyclopentadienyl iron(II), 99.5%, Strem) were purified via sublimation. Ferrocenium tetrafluoroborate ($\text{Fc}^+[\text{BF}_4]^-$, bis(cyclopentadienyl)iron(III) tetrafluoroborate, technical grade, Sigma-Aldrich) was recrystallized from a mixture of diethyl ether (ACS grade, EMD) and acetonitrile (ACS grade, EMD) and dried under vacuum. Cobaltocenium hexafluorophosphate (CoCp_2^+ , bis(cyclopentadienyl)cobalt(III) hexafluorophosphate, 98%, Sigma-Aldrich) was recrystallized from a mixture of ethanol (ACS grade, EMD) and acetonitrile (ACS grade, EMD) and dried under vacuum. Acetylferrocenium (AcFc^+) was generated in situ via electrochemical oxidation of AcFc^0

with the concomitant reduction reaction occurring in a compartment that was separated by a Vycor frit from the working electrode compartment. Potassium ferricyanide ($\text{K}_3[\text{Fe}(\text{CN})_6]$, 99.2%, Sigma-Aldrich) and potassium ferrocyanide ($\text{K}_4[\text{Fe}(\text{CN})_6] \cdot 3\text{H}_2\text{O}$, ACS Certified, Fischer Scientific) were used as received. LiClO_4 (battery grade, Sigma-Aldrich) was used as received. Petri dishes used were Falcon Optilux™ branded and were cleaned with water prior to use. All other chemicals were used as received unless otherwise noted.

5.6.1.2 Electrode fabrication

Monolayer graphene was grown by chemical-vapor deposition (CVD) of carbon on Cu.¹ Additional CVD-grown monolayer graphene on Cu was purchased from Advanced Chemical Supplier Materials.

A 2.5 cm x 1 cm piece of monolayer graphene on Cu (from either source) was fluorinated using a home-built XeF_2 pulse chamber, with one pulse of XeF_2 (g) at 2 Torr for 90 s with a base pressure of <1 mTorr. The fluorinated graphene samples on Cu were then coated with 495K A4 polymethyl methacrylate (PMMA, MicroChem) by spinning at 2000 rpm (500 rpm s^{-1} acceleration) for 60 s, followed by a 5 min bake at 185 °C. This procedure was repeated twice to yield a PMMA/F-Gr/Cu stack.

Smaller pieces were cut from the PMMA/F-Gr/Cu and floated in FeCl_3 solution until complete removal of the Cu (~1 h) was observed. To remove the etchant residue, each stack was transferred between five consecutive $\geq 18\text{M}\Omega\text{-cm}$ resistivity water baths. N-type Si was etched for 30 s in buffered improved HF (Transene) to yield n-Si-H surfaces, and any SiO_2 was removed using a modified SC1/SC2 cleaning method. SC-1 consisted of soaking the Si wafers in a 5:1:1 (by volume) solution of H_2O , NH_4OH (~30

wt.%, J.T. Baker) and H_2O_2 (~35 wt.%, Sigma) for 10 min at 75 °C. After washing with H_2O , SC-1 cleaned wafers were exposed to SC-2 conditions, which consisted of soaking the Si wafers in a 5:1:1 (by volume) solution of H_2O , HCl (11.1 M, Sigma) and H_2O_2 (~35 wt.%, Sigma) for 10 min at 75 °C. A clean PMMA/F-Gr stack was then pulled gently onto the appropriate Si wafer and dried with a stream of $\text{N}_2(\text{g})$ to remove any remaining water between the Si wafer and the graphene sheet. The final PMMA/F-Gr/wafer stack was baked at 80 °C for 10 min in air. The majority of the PMMA was detached with a 10 min acetone soak and the remaining PMMA residue was removed by an anneal ($\text{H}_2:\text{Ar}$ v:v 5:95) for 2h at 350 °C.²

Si/F-Gr electrodes were fabricated using Ga:In (75:25) eutectic as an ohmic back contact. The wafers were attached to a Cu wire with Ag paint (high purity, SPI Supplies). All surfaces except the F-Gr layer were covered with insulating epoxy (Loctite Hysol 9460). CH_3 -terminated Si(111) wafers were prepared using a previously reported procedure.³ H-terminated Si(111) electrodes were etched with HF(aq) immediately before use.

5.6.1.3 Instrumentation

X-ray photoelectron spectroscopic (XPS) data were collected at $\sim 5 \times 10^{-9}$ Torr using a Kratos AXIS Ultra DLD with a magnetic immersion lens that consisted of a spherical mirror and concentric hemispherical analyzers with a delay-line detector (DLD). An Al $K\alpha$ (1.486 KeV) monochromatic source was used for X-ray excitation. Ejected electrons were collected at a 90° angle from the horizontal. The CASA XPS software package v 2.3.16 was used to analyze the collected data.

Raman spectra were collected with a Renishaw Raman microscope at $\lambda=532$ nm through an objective with numerical aperture=0.75. The laser power was ~ 3 mW.

UV/Vis transmission spectra were collected with a Cary 5000 absorption spectrometer equipped with an external DRA 1800 attachment. The data were automatically zero/baseline corrected by the instrument before any additional processing was performed.

Electrochemical data were obtained using a Princeton Applied Research Model 273, Biologic SP-250, or a Gamry Reference 600 potentiostat. A Pt wire reference electrode (0.5 mm dia., 99.99% trace metals basis, Sigma-Aldrich) and a Pt mesh counter electrode (100 mesh, 99.9% trace metals basis, Sigma-Aldrich) were used for the electrochemical measurements. The cell potentials for the nonaqueous redox species were determined using cyclic voltammetry to compare the solution potential to the formal potential of the redox species. The potential difference between cells was calculated using the difference between the formal potentials for each redox couple in conjunction with standard reduction potentials from the literature. The $\text{CH}_3\text{CN-CoCp}_2^{+/0}$ solution (CoCp_2 [3 mM]/ CoCp_2^+ [50 mM]) was calculated to have a solution potential of $E(\text{A}/\text{A}^-) = -1.26$ V vs Fc/Fc^+ , the $\text{CH}_3\text{CN-Fc}^{+/0}$ solution (Fc [55 mM]/ Fc^+ [3 mM]) was calculated to have $E(\text{A}/\text{A}^-) = -0.10$ V vs Fc^+/Fc , and the $\text{CH}_3\text{CN-AcFc}^{+/0}$ solution (pre-electrolysis AcFc concentration = [50 mM]) was calculated to have $E(\text{A}/\text{A}^-) = +0.40$ V vs Fc^+/Fc . The nonaqueous electrochemical solutions each contained 1.0 M LiClO_4 . The aqueous 50 mM $\text{K}_3[\text{Fe}(\text{CN})_6]$ - 350 mM $\text{K}_4[\text{Fe}(\text{CN})_6]$ solution contained no additional supporting electrolyte due to the high intrinsic salt concentration. The current under forward bias saturated at much larger values in the $\text{Fe}(\text{CN})_6^{3-/4-}$ solution than in the Fc^+/Fc solution due

of the increased concentration of electron-accepting species in the $\text{Fe}(\text{CN})_6^{3-/4-}$ solution. $\text{Fc}[\text{BF}_4]$ is a highly colored species that, at high concentrations, absorbs a significant fraction of the light prior to photons striking the photoelectrode. The electrolyte solution was rapidly stirred with a small, Teflon-covered stir bar. Illumination was provided with an ENH-type tungsten-halogen lamp. Illumination intensities were set to provide $\sim 10\text{-}11$ mA cm^{-2} of light-limited current density. These intensities corresponded to $\sim 1/3$ rd of a Sun (~ 33 mW cm^{-2}), respectively, as determined through the concurrent use of a Si photodiode (Thor Laboratories) that was calibrated relative to a secondary standard photodetector that was NIST-traceable and calibrated at 100 mW cm^{-2} of AM1.5G illumination. Nonaqueous electrochemistry was performed anaerobically in an $\text{Ar}(\text{g})$ -filled glovebox. Aqueous electrochemistry was performed in air. Electrodes were washed with H_2O and dried prior to transfer between electrolyte solutions.

The current density versus potential data in $\text{HBr}(\text{aq})$ were measured using a three-electrode setup with a Si working electrode, a Pt wire pseudo-reference electrode, and a large Pt mesh counter electrode. The electrolyte consisted of aqueous 0.4M Br_2 - 7.0 M HBr ($\text{pH}=0$) electrolyte under rapid stirring, and ~ 33 mW cm^{-2} of simulated solar illumination from an ELH-type W-halogen lamp.

Photoelectrochemical deposition of Pt was performed by immersing the electrode into an aqueous solution of 5 $\text{mM K}_2\text{PtCl}_4$ (99.9%, Alfa Aesar) and 200 mM LiCl . Using a three-electrode setup, with a saturated calomel reference electrode and a Pt mesh counter electrode, galvanostatic control was maintained at -0.1 mA/cm^2 in a stirred solution until -100 mC/cm^2 had passed. The samples were then rinsed with deionized water and were dried under a stream of $\text{N}_2(\text{g})$.

5.6.2 Supporting Data

5.6.2.1 Electrochemical behavior of $\text{np}^+\text{-Si/F-Gr}$ electrodes in aqueous solution

Figure 5A.1 displays the stability data before normalization. The first and last CV for each electrode is also shown. The CVs are not corrected for loss of light-limited current. The current density decay seen in the original chronoamperograms is due to solution decay and fluctuations in the light source as the light-limited current at very positive potentials (+0.4 V) decreased over time, leading to the normalization present in the main text.. Overall, there is little change to the E_{OC} , J_{SC} , and ff for either the n-Si or np^+Si electrodes before and after testing for 100 ks.

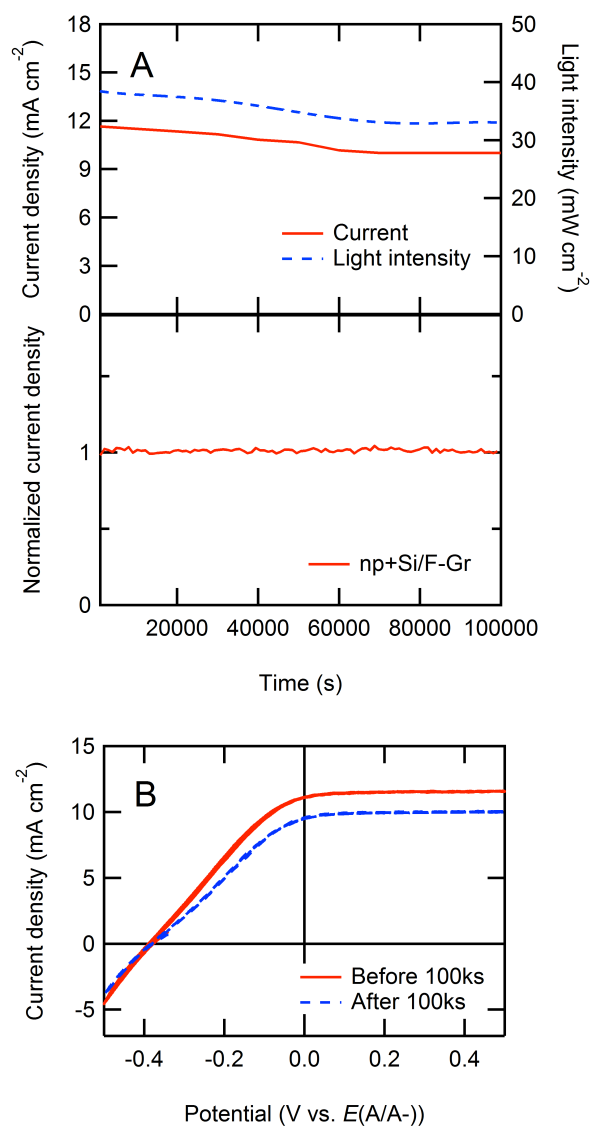


Figure 5A.1. Current density vs. time ($J-t$) and current density vs. potential ($J-E$) behavior of $\text{np}^+\text{-Si/F-Gr}$ electrodes in contact with aqueous 50 mM $\text{Fe}(\text{CN})_6^{3-}$ - 350 mM $\text{Fe}(\text{CN})_6^{4-}$ electrolyte under $\sim 33 \text{ mW cm}^{-2}$ of ENH-type W-halogen illumination. (A) The $J-t$ behavior of $\text{np}^+\text{-Si/F-Gr}$ at $E = 0 \text{ V vs. } E(\text{A/A}^-)$ over 100,000 s ($>24 \text{ h}$). The normalized current density is reported to correct for any variations in the light intensity during the experiment. (B) $J-E$ behavior of $\text{np}^+\text{-Si/F-Gr}$ (3 scans at 50 mV s^{-1}) before and after exposure to the conditions depicted in (A). The current

density decay in the original chronoamperograms is consistently ascribed to fluctuations in the light source, as well as to decomposition of the $\text{Fe}(\text{CN})_6^{3-/4-}$ under illumination, which produced thin colored film on the electrochemical cell over the course of the experiment depicted in (A).

5.6.2.2 Comparison of graphene-imparted stability between graphene growths

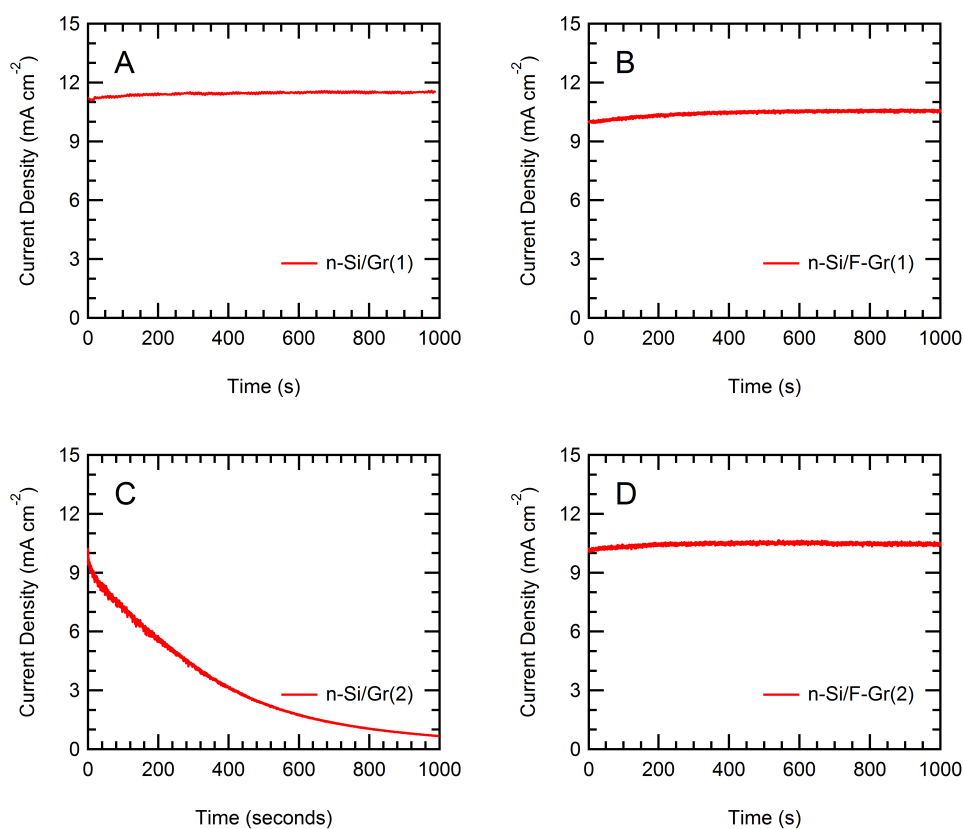


Figure 5A.2. *J-t* data for n-Si/Gr and n-Si/F-Gr electrodes from two different graphene growths in contact with aqueous 50 mM Fe(CN)₆³⁻ - 350 mM Fe(CN)₆⁴⁻ under ~33 mW cm⁻² of W-halogen illumination. (A) The n-Si/Gr from the first graphene sheet (growth 1) exhibited stable current densities for > 1000 s. (B) Fluorination of graphene from growth 1 yielded n-Si/F-Gr electrodes that exhibited stable current densities for > 1000 s. (C) Another graphene growth (growth 2) yielded n-Si/Gr electrodes that did not exhibit stable current densities for > 1000 s. (D) When Batch 2 was fluorinated, the n-Si/F-Gr electrodes exhibited stable current densities for > 1000 s. The behavior is consistent with expectations for the stabilization of otherwise unstable graphene arising from fluorine termination of high-energy defect sites in the graphene lattice.

Figure 5A.2 shows that graphene from a CVD growth which exhibited fast decay of current density over the first 1000s of testing in the $\text{Fe}(\text{CN})_6^{3/4-}$ couple, can be stabilized by fluorination. The same piece of graphene-covered copper foil was cut into multiple pieces, of which one was fluorinated and the other was not. Several of the electrodes made on n-Si-H from the graphene that was not fluorinated showed a rapid decay over 1000s. However, electrodes made on n-Si-H from the fluorinated graphene demonstrated stability over the same 1000s. We postulate that this ability to stabilize otherwise unstable graphene comes from fluorine termination of high-energy defect sites in the graphene lattice. This passivation of reactive sites increases the stability of the graphene sheet.

5.6.2.3 X-ray Photoelectron Spectroscopy of Fluorinated Graphene

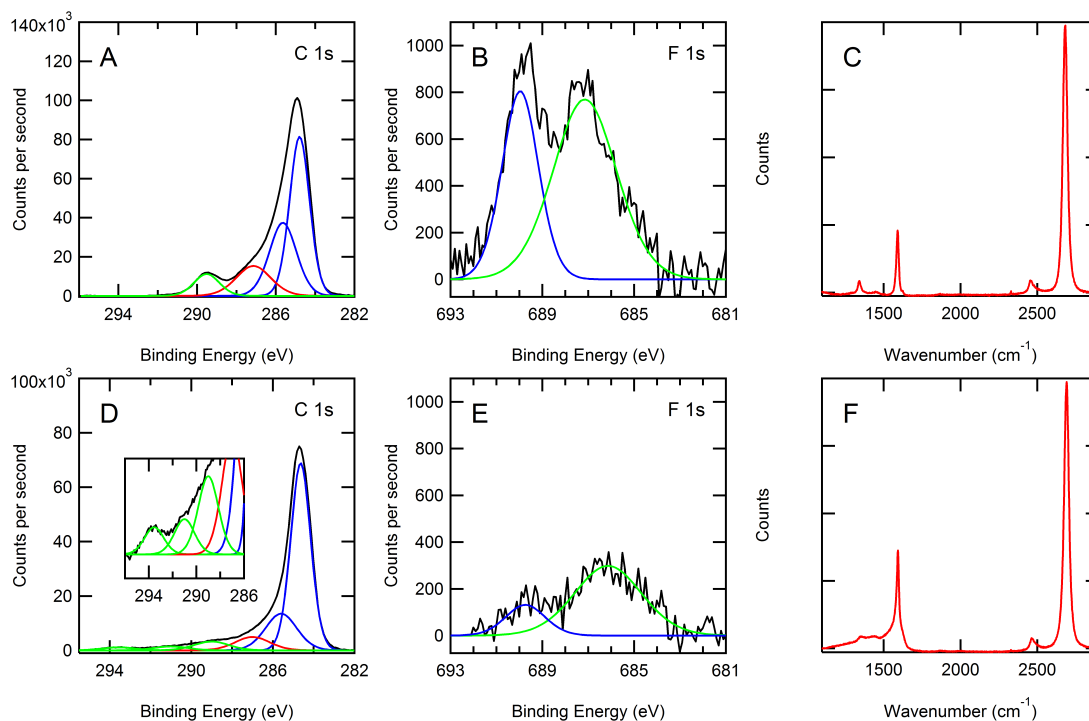


Figure 5A.3 Raman and X-ray photoelectron (XP) spectra of fluorinated graphene (F-Gr) before and after annealing. (A) The C 1s region before annealing displayed four peaks at binding energies of 284.8 eV, 285.6 eV, 287.2 eV, and 289.5 eV, respectively. Peaks attributed to carbon bound to fluorine are shown in green; peaks attributed to carbon bound to carbon are shown in blue; and peaks attributed to carbon bound to oxygen are shown in red. (B) The F 1s region displayed two peaks at binding energies of 687.1 eV and 690.0 eV, respectively. (C) The Raman spectra before annealing showed a prominent defect peak at 1350 cm^{-1} . (D) Two additional peaks, at 291 eV and 293.5 eV (inset), attributable to CF_2 and CF_3 groups, were observed in the C 1s XP spectra after annealing. (E) The positions of the peaks in the F 1s region were shifted slightly to 686.1 eV and 689.8 eV, respectively, and decreased in size. (F) The defect peak at 1350 cm^{-1} broadened after the anneal. These spectra are consistent with a lightly fluorinated (C_xF_y , $x > 10$) graphene surface.⁴ The change in fluorination profile after annealing is consistent with a reorganization of the fluorine on the surface, and the XPS spectra demonstrate the expected decrease in fluorine content after a two-hour 350 °C anneal under a H_2 :Ar (5:95) atmosphere.⁴

5.6.2.4 Chemical stability of fluorinated graphene in aqueous solutions of varying pH (0,7,14)

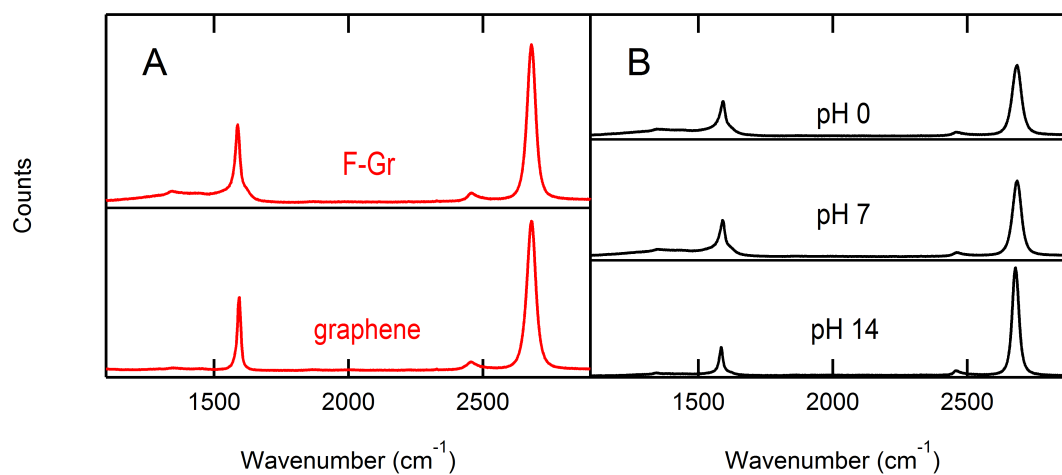


Figure 5A.4. Stability tests of F-Gr in acidic (1 M HCl), alkaline (1 M KOH), and neutral (deionized water) conditions. An initial Raman of the pristine graphene sheets before fluorination and after fluorination showed an increase in the size of the defect peak at 1350 cm⁻¹. This defect peak remained unchanged after 1 h in acidic or neutral solutions. In contrast, immersion for 1 h in alkaline media produced a decrease in the density of the defect peak.

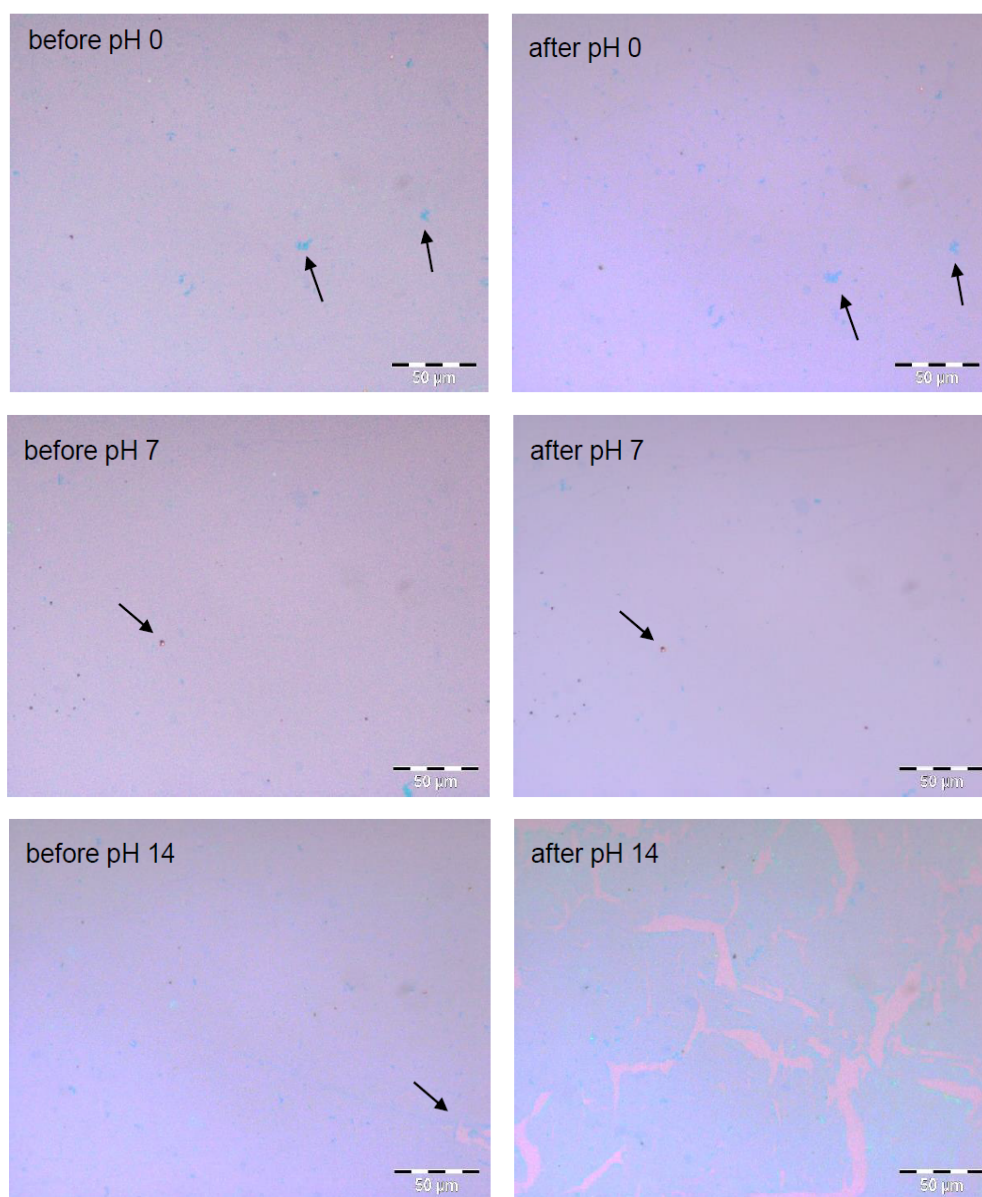


Figure 5A.5. Optical images of stability tests of F-Gr in acidic (1 M HCl), alkaline (1M KOH), and neutral (deionized water) conditions. Arrows indicate points of reference for the corresponding before and after images.

The stability of the fluorinated graphene was tested under acidic, neutral, and alkaline aqueous solutions, respectively. To insure that the same area was examined before and after testing, a small area on the graphene wafer was outlined with Hysol 9460 epoxy. Optical images along with Raman spectra were acquired, and wafers were then placed for 1 h in aqueous solutions at pH 0, pH 7, and pH 14. After carefully rinsing the samples with $>18 \text{ M}\Omega\text{-cm H}_2\text{O}$ and drying the samples with a stream of $\text{N}_2(\text{g})$, optical images along with Raman spectra were obtained from the same areas as before testing. The Raman spectra and optical images of the samples soaked in acidic and neutral solutions showed no change after testing (Figure 5A.4). The samples tested in alkaline solutions showed a marked decrease in defect density of the remaining sections of fluorinated graphene, closely mimicking the profile of pristine graphene. Repeated tests of fluorinated graphene in 1 M KOH(aq) showed large-scale delamination of the fluorinated graphene sheet, as observed in the images before and after exposure to the aqueous pH 14 solution.

5.6.2.5 UV-Vis Spectroscopy of Graphene and Fluorinated Graphene

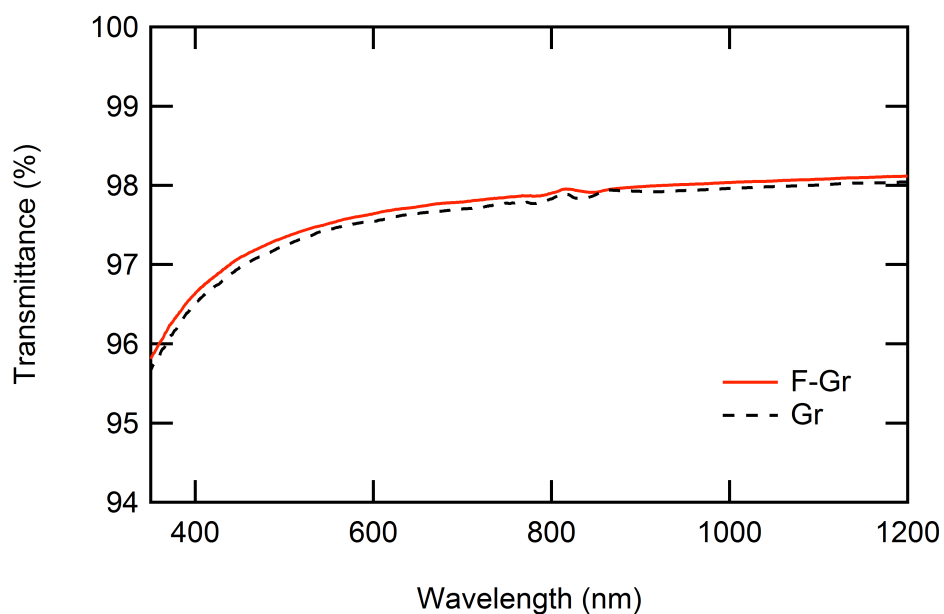


Figure 5A.6. UV/Vis spectra of Gr and F-Gr on glass. Graphene and fluorinated graphene were transferred to borosilicate glass slides using the standard transfer procedures (*vide supra*). The slightly increased transmission for F-Gr is consistent with the expectation of decreased visible light absorption upon fluorination of graphene.

5.6.2.6 Inhibition of platinum silicide formation

XP spectra of Si-Me/F-Gr/Pt and Si-Me/Pt surfaces were obtained to investigate the ability of F-Gr to inhibit platinum silicide formation. Pt was deposited at ~3 nm thickness via electron-beam evaporation on both F-Gr covered and bare Si surfaces. The 3 nm Pt thickness was chosen to allow for interrogation of the sample surface to a depth at which both Si and Pt were observable by XPS. Methylated Si surfaces were used to inhibit the formation of Si oxide at the Si/Pt interface during sample fabrication, because Si oxide of sufficient thickness is also capable of preventing silicide formation.⁶ Figure 5A.7a shows the XP spectrum of a pure Pt phase. A thicker Pt layer (20 nm) was used to interrogate only the pure Pt phase. Figure 5A.7b shows the Pt 4f XP spectrum of CH₃-terminated Si with a 3 nm Pt overlayer. The Pt 4f peak shifted to higher binding energy, indicative of platinum silicide formation.⁵ The shoulder of the peak at low binding energy is consistent with a pure Pt phase overlayer. Conversely, 3 nm of Pt on F-Gr covered silicon showed essentially no change in the Pt 4f binding energy immediately after fabrication (Figure 5A.7c) or after a 1 h anneal under forming gas at 300 °C (Figure 5A.7d). The data are thus indicative of little or no platinum silicide formation. Figure 5A.7e presents an overlay of the spectra in Figure 5A.7a-5A.7d and highlights the difference between the Pt 4f peak positions.

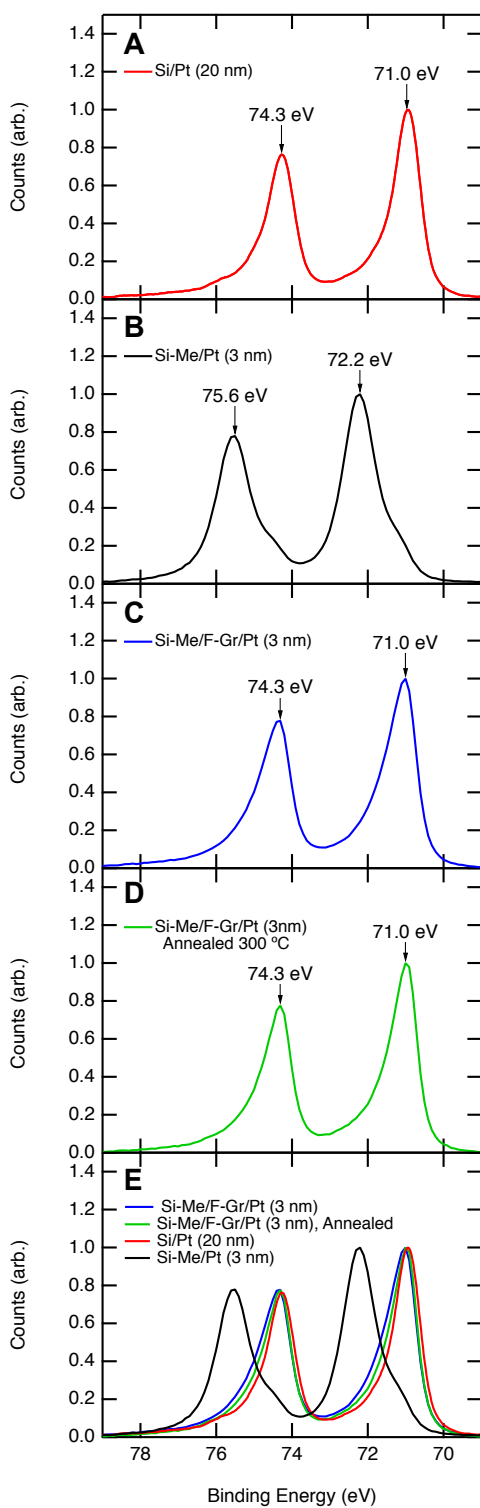


Figure 5A.7. The Pt 4f XP spectra of Pt on both F-Gr covered and Si surfaces. (A) XP spectrum of a thick (20 nm) layer of Pt on Si. This spectrum is representative of a pure Pt phase. (B) XP spectrum of a 3 nm layer of Pt on Si. The Pt 4f peak shifted to high binding energy (72.2 and 75.6 eV), characteristic of platinum silicide formation.⁵ The shoulder to lower binding energy is attributed to a pure Pt phase. (C) XP spectrum of Si-Me/F-Gr/Pt (3 nm). The Pt 4f peak positions (71.0 and 74.3 eV) are consistent with pure Pt. (D) XP spectrum of Si-Me/F-Gr/Pt after annealing at 300 °C under forming gas. (E) Overlay of XP spectra (A)-(D).

5.2.6.7 n-Si/F–Gr non-aqueous photoelectrochemistry

Table S1. E_{oc} values for n-Si/Gr and n-Si/F–Gr electrodes in contact with non-aqueous redox couples under $\sim 33 \text{ mW cm}^{-2}$ of W-halogen illumination. The Nernstian potential, $E(A/A^-)$, of the contacting non-aqueous electrolytes were measured as follows:

$E(\text{CoCp}_2^{+/0}) = -1.26 \text{ V vs. } E^{\circ'}(\text{Fc}^{+/0})$, $E(\text{Fc}^{+/0}) = -0.1 \text{ V vs. } E^{\circ'}(\text{Fc}^{0/+})$, $E(\text{AcFc}^{+/0}) = +0.4 \text{ V vs } E^{\circ'}(\text{Fc}^{+/0})$.

	$E_{oc,\text{CoCp}_2^{+/0}}$ (V vs. $E(\text{CoCp}_2^{+/0})$)	$E_{oc,\text{Fc}^{+/0}}$ (V vs. $E(\text{Fc}^{+/0})$)	$E_{oc,\text{AcFc}^{+/0}}$ (V vs. $E(\text{AcFc}^{+/0})$)
Gr	0	0.26	0.43
F–Gr	0	0.20	0.30

5.6.2.8 H-Br stability/efficiency over time

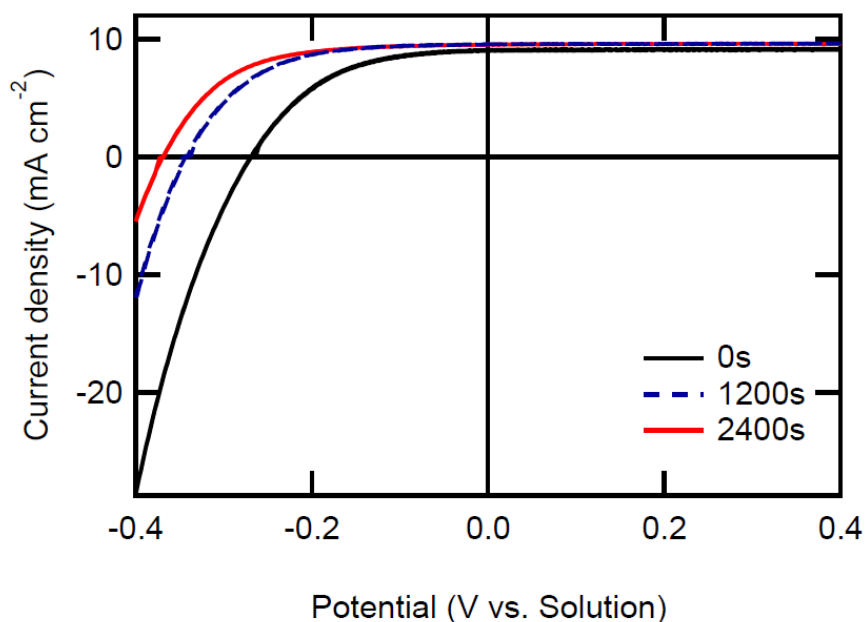


Figure 5A.8. Current density-potential (J - E) behavior of an n-Si/F-Gr/Pt photoanode before, during, and after 2400 s of photoelectrochemical stability testing in contact with 0.4M Br₂ - 7.0 M HBr (pH=0) aqueous electrolyte. Photoelectrochemical stability was measured by observing the J - t behavior at an initial current density of 10 mA cm⁻² over the specified time period (see Figure 5.3). The behavior of the n-Si/F-Gr/Pt electrode improved over 2400 s, with improvements in E_{oc} (0.27 V to 0.37 V), J_{SC} (9.0 mA to 9.5 mA), and ff (0.51 to 0.59), resulting in an increase in the ideal regenerative cell conversion efficiency from 3.5% to >5%.

5.6.2.9 XPS Oxide Analysis

XPS analysis was performed in order to determine the effect of electrochemical oxidation at the Si–Me surface on the oxidation state of the Si photoanode surface (Figure 5.2). Silicon oxide detected before and after electrochemical oxidation was quantified using a simple substrate—overlayer model described by equation 1:⁷

$$d = \lambda_{ov} \sin \theta \left\{ \ln \left[1 + \frac{I_{Si}^o}{I_{ov}^o} * \frac{I_{ov}}{I_{Si}} \right] \right\} \quad (1)$$

Where d is the overlayer thickness, λ_{ov} is the attenuation factor through the oxide overlayer (assumed to be 2.6 nm)⁸, θ the angle from the surface of the sample to the detector (90°), $\frac{I_{Si}^o}{I_{ov}^o}$ is an instrument normalization factor related to the expected signal for a pure Si and a pure SiO₂ sample (taken to be 1.3 for this instrument), I_{ov} is the measured intensity of the silicon, and I_{Si} is the measured intensity of the silicon oxide overlayer. The thickness of a monolayer of oxide was taken to be 0.35 nm.⁹ Negligible silicon oxide was detected on the bare methyl-terminated silicon surfaces prior to electrochemical oxidation (Figure 5.2a) and an oxide thickness of approximately 0.75 nm, or >2 monolayers of oxide, was observed after exposure of the Si–Me surface (Figure 5.2b) to the electrochemical oxidation conditions described in Figure 5.2. An oxide thickness of approximately 0.15±0.05 nm was detected on the Si–Me/F–Gr surfaces prior to electrochemical oxidation (Figure 5.2c) and an oxide thickness of approximately 0.17±0.5 nm, was observed after exposure (Figure 5.2d) of the Si–Me/F–Gr surface to the electrochemical oxidation conditions described in Figure 5.2.

5.6.3 Appendix References

1. N. Petrone, C. R. Dean, I. Meric, A. M. van der Zande, P. Y. Huang, L. Wang, D. Muller, K. L. Shepard and J. Hone, *Nano Lett.*, 2012, **12**, 2751-2756.
2. A. Pirkle, J. Chan, A. Venugopal, D. Hinojos, C. W. Magnuson, S. McDonnell, L. Colombo, E. M. Vogel, R. S. Ruoff and R. M. Wallace, *Appl. Phys. Lett.*, 2011, **99**, -.
3. N. T. Plymale, Y.-G. Kim, M. P. Soriaga, B. S. Brunschwig and N. S. Lewis, *J. Phys. Chem. C*, 2015, **119**, 19847-19862.
4. R. Stine, W.-K. Lee, K. E. Whitener, J. T. Robinson and P. E. Sheehan, *Nano Lett.*, 2013, **13**, 4311-4316.
5. G. Larrieu, E. Dubois, X. Wallart, X. Baie and J. Katcki, *J. Appl. Phys.*, 2003, **94**, 7801.
6. J. R. Abelson, K. B. Kim, D. E. Mercer, C. R. Helms, R. Sinclair and T. W. Sigmon, *J. Appl. Phys.*, 1988, **63**, 689-692.
7. D. Briggs and M. P. Seah, *Practical Surface Analysis*, John Wiley & Sons Ltd, 2nd edn., 1990.
8. M. F. Hochella Jr and A. H. Carim, *Surface Science*, 1988, **197**, L260-L268.
9. J. A. Haber and N. S. Lewis, *J. Phys. Chem. B*, 2002, **106**, 3639-3656.